Boosting Sodium Storage of $Fe_{1-x}S/MoS_2$ Composite via Heterointerface Engineering

Song Chen[1,2], Shaozhuan Huang[2], Junping Hu[2], Shuang Fan[1,2], Yang Shang[2],
Mei Er Pam[2], Xiaoxia Li[2], Ye Wang[4], Tingting Xu[4], Yumeng Shi[1,3] ✉, Hui Ying Yang[2] ✉

✉ Yumeng Shi, yumeng_shi@163.com; Hui Ying Yang, yanghuiying@sutd.edu.sg

[1] International Collaborative Laboratory of 2D Materials for Optoelectronics Science and Technology
of Ministry of Education, College of Optoelectronic Engineering, Shenzhen University, Shenzhen 518060,
People's Republic of China

[2] Pillar of Engineering Product Development, Singapore University of Technology and Design, 8 Somapah
Road, Singapore 487372, Singapore

[3] Engineering Technology Research Center for 2D Material Information Function Devices and Systems
of Guangdong Province, College of Optoelectronic Engineering, Shenzhen University, Shenzhen 518060,
People's Republic of China

[4] Key Laboratory of Material Physics of Ministry of Education, School of Physics and Engineering,
Zhengzhou University, Zhengzhou 450052, People's Republic of China

HIGHLIGHTS

- $Fe_{1-x}S/MoS_2$ heterostructure with abundant "ion reservoir" interfaces is designed to reduce sodium ion diffusion barrier and facilitate charge-transfer kinetics, thus endowing the electrode with excellent cycling stability and rate capability.

- The in-depth analysis on the dynamic relationship between heterointerface and sodium storage performance carves a new path for interface engineering toward the next-generation high-performance energy storage devices.

ABSTRACT Improving the cycling stability of metal sulfide-based anode materials at high rate is of great significance for advanced sodium ion batteries. However, the sluggish reaction kinetics is a big obstacle for the development of high-performance sodium storage electrodes. Herein, we have rationally engineered the heterointerface by designing the $Fe_{1-x}S/MoS_2$ heterostructure with abundant "ion reservoir" to endow the electrode with excellent cycling stability and rate capability, which is proved by a series of in and ex situ electrochemical investigations. Density functional theory calculations further reveal that the heterointerface greatly decreases sodium ion diffusion barrier and facilitates charge-transfer kinetics. Our present findings not only provide a deep analysis on the correlation between the structure and performance, but also draw inspiration for rational heterointerface engineering toward the next-generation high-performance energy storage devices.

$Fe_{1-x}S/MOS_2$ heterostructure

Interface

$Fe_{1-x}S$ MoS_2

Na^+ reservoir

Facilitated sodium ion diffusion
Enhanced charge transfer kinetics

KEYWORDS Heterostructure; Heterointerface; Diffusion barrier; Ion reservoir; Sodium ion battery
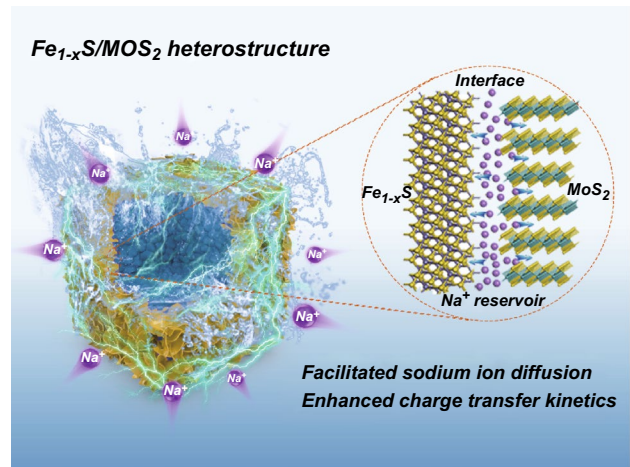
1 Introduction

Sodium ion batteries (SIBs) have aroused great interests as a promising substitute to conventional lithium ion batteries (LIBs) owing to the overwhelming superiority in low cost and abundant natural resources [1–4]. However, the sluggish reaction kinetics induced by the larger ionic radius of Na ions deteriorates their electrochemical properties seriously [5, 6]. The key point to achieve high-performance SIBs relies on the rational design of electrode materials with satisfactory Na ions insertion/extraction performance during repeated cycles, especially for the active anode host materials. Among the various anode materials, transition metal sulfides (M_xS_y) have drawn extensive attentions due to their high sodium storage capacity [7–10]. Moreover, the weaker M–S bond than M–O bond is more kinetically favorable for electrochemical conversion reaction, leading to a better redox kinetics and reversibility [11]. As a typical example, iron sulfide ($Fe_{1-x}S$) has risen to prominence because of its high theoretical capacity (~ 610 mAh g^{-1}), natural abundance and environmental benignity [12, 13]. Nonetheless, there are still obstacles to its commercial applications mainly due to the poor intrinsic conductivity and severe volume changes during the sodiation/desodiation processes, thus resulting in inferior cycling stability and rate capability [14]. Besides $Fe_{1-x}S$, 2D layered molybdenum disulfide (MoS_2) is another promising anode candidate for SIBs due to its analogous structures to graphite [15–17]. In particular, the large interlayer spacing (0.62 nm) and high mechanical strength of MoS_2 are able to facilitate Na$^+$ migration and alleviate structural deformation during the discharge/charge processes [18]. Considering the advantages of these two metal sulfides, a hybrid composite by combining $Fe_{1-x}S$ with MoS_2 can be rationally designed and fabricated to expectedly achieve the desirable performance.

Constructing unique heterostructures to create diverse interface effects offers unprecedented opportunities in various fields, such as solar cells, photocatalysis and electrocatalysis [19–27]. The heterointerfaces deriving from coupling nanostructures with different properties can greatly accelerate charge transport and improve reaction kinetics [28]. Nishitani et al. [29] have studied the charge-transfer effects in CdO/SnTe heterointerfaces, which revealed a large fourfold enhancement of electron mobility. Yin et al.

[30] have investigated the charge carrier transfer in the bulk heterostructures and indicated the balanced hole/electron mobilities are key factors to attribute high solar cell performance. Hints from the previous reports indicate that rational interface designing could be of great importance for the improvement of conversion reaction kinetics in rechargeable SIBs. Some emerging heterostructures such as Ni_3S_2/MoS_2, Sb_2S_3/SnS_2 and Sb_2S_3/MoS_2 have demonstrated outstanding electrochemical performance, which is difficult to realize in a signal material system [31–36]. However, the detailed synergistic effects and heterointerface properties are rarely revealed.

Herein, we design a $Fe_{1-x}S/MoS_2$ heterostructure with abundant "ion reservoir" to provide fast Na$^+$ diffusion channels and interpret specifically the correlation between heterointerface and sodium ion diffusion. The DFT calculations further confirm that the heterointerface significantly reduces the diffusion barrier and facilitates the charge-transfer kinetics, hence enabling excellent cycling stability and rate capability. Our findings not only provide in-depth understanding of the dynamic relationship between heterointerface and electrochemical performance, but also carve a new path for engineering rationally heterostructures toward high-performance energy storage devices.

2 Experimental Section

2.1 Material Preparation

Synthesis of the Prussian blue (PB) nanocubes. PB nanocubes were synthesized by a hydrothermal method reported previously with modifications [37]. In a typical process, 12 g polyvinylpyrrolidone (PVP, MW $\approx 40,000$) and 0.6 g potassium hexacyanoferrate (II) ($K_4Fe(CN)_6\cdot 3H_2O$) were added into 0.1 M hydrochloric acid (HCl, 37%) under magnetic stirring, to form a clear solution. Subsequently, the solution was transferred in a programmable oven and then heated to 80 °C for 24 h. Finally, PB nanocubes were obtained by centrifuging and washing with water and ethanol and then dried in a vacuum oven overnight.

Synthesis of nitrogen-doped porous nanocubic structure (FeCN). FeCN nanocubes were obtained by calcining the as-synthesized PB nanocubes at 500 °C for 4 h under argon flow with a heating rate of 1 °C min^{-1}.

Synthesis of FeCN/MoS$_2$ nanocomposite. Twenty-five milligrams of FeCN nanocubes was dispersed in a mixed solvent containing 15 mL dimethylformamide and 15 mL ethanol under ultrasonication for 30 min. Then, 50 mg of ammonium tetrathiomolybdate ((NH$_4$)$_2$MoS$_4$) was added to the above suspension under magnetic stirring. After stirring for 12 h, the mixture was transferred into a Teflon-lined stainless-steel autoclave and heated at 210 °C for 10 h. Then, the autoclave was cooled to room temperature naturally. The obtained FeCN/MoS$_2$ nanocomposite was centrifuged and washed with water and ethanol for several times, and dried in a vacuum oven at 80 °C overnight.

Synthesis of Fe$_{1-x}$S/MoS$_2$ nanocomposite. The as-prepared FeCN/MoS$_2$ composite and sodium hydrosulfide (NaHS·H$_2$O) as sulfurization precursor were placed in an alumina boat that was inserted into a tubular furnace. Subsequently, the tubular furnace was heated to 400 °C for 4 h and then heated to 600 °C for 2 h under argon flow with a heating rate of 2 °C min^{-1}. Finally, Fe$_{1-x}$S/MoS$_2$ nanocomposite was obtained.

For comparison, bare Fe$_{1-x}$S nanocubes were synthesized through the same method without (NH$_4$)$_2$MoS$_4$ in similar conditions.

2.2 Material Characterization

Crystal structure of all samples was performed by X-ray diffraction techniques (XRD, Bruker D8 Advance) with Cu Kα radiation operated at 40 kV and 25 mA. The morphology and microstructure were observed using field emission scanning electron microscope (FESEM, JEOL JSM-7600F), transmission electron microscopy and high-resolution transmission electron microscopy (TEM and HRTEM, JEOL JEM-2010). The surface electronic states were analyzed by X-ray photoelectron spectroscopy (XPS, PHI Quantera II) with Al Kα source operated at 1486.6 eV. Nitrogen adsorption–desorption isotherms were carried out on a Quantachrome Autosorb-IQ analyzer. For in situ XRD measurement, each scan was collected between 10° and 50° using an electrochemical cell module equipped with metal beryllium (Be) and carbon paper as the window and current collector, respectively.

2.3 Electrochemical Measurements

To fabricate working electrodes, active materials (Fe$_{1-x}$S/MoS$_2$ or Fe$_{1-x}$S), acetylene black and carboxymethyl cellulose (CMC) at a weight ratio of 7:2:1 were dispersed in deionized water to form a homogeneous slurry. The resultant slurry was coated on the copper foil and then dried at 120° for 12 h in a vacuum oven. In a typical assembly process of CR2032 coin cells, sodium foil was used as the reference and counter electrodes, and glass fibers (GF, Whatman) were used as separators. 1 M NaPF$_6$ was dissolved into a mixed solution of ethylene carbonate (EC) and diethyl carbonate (DEC) (EC/DMC, 1:1/v: v) with 2.5 wt% fluoroethylene carbonate (FEC) as electrolyte. The galvanostatic charge/discharge tests were conducted on a battery testing system (Neware) at different densities in a voltage range of 0.01–3.0 V. Cyclic voltammetry (CV) was carried out using an electrochemical workstation (VMP3, Bio-Logic) at different scan rates. Electrochemical impedance spectroscopy (EIS) was performed on the same workstation in a frequency range from 100 kHz to 10 mHz.

2.4 DFT Calculations

All the calculations are based on density functional theory (DFT) using the plane-wave pseudopotentials [38, 39] with exchange–correlation of Perdew–Burke–Ernzerhof (PBE) [40, 41] formation as implemented in the Vienna Ab initio Simulation Package (VASP) [42]. A cutoff energy of 450 eV is employed for the plane-wave expansion of the wave functions. The Brillouin zone is sampled with $3 \times 3 \times 1$ Monkhorst–Pack k-point mesh [43] for the structural optimization. The convergence criteria for the total energy and ionic forces were set to 10^{-4} eV and 0.1 eV Å^{-1}, respectively. The construction with a 20 Å vacuum zone in the z direction to minimize the interactions between adjacent images. The climbing-image nudged elastic band (NEB) method [44] is used to seek the minimum energy pathways and determine the diffusion energy barriers.

3 Results and Discussion

The synthetic procedures for the Fe$_{1-x}$S/MoS$_2$ nanocomposite are illustrated in Fig. 1a. PB nanocubes were first synthesized using a simple hydrothermal method. The as-prepared PB shows the typical diffraction peaks ascribed to Fe$_4$[Fe(CN$_6$)]$_3$ with a face-centered-cubic structure (JCPDS NO. 73-0687) and a well-defined nanocubic morphology with an average size of about 700 nm (Fig. S1a, b). Next, PB nanocubes were pyrolyzed to nitrogen-doped porous
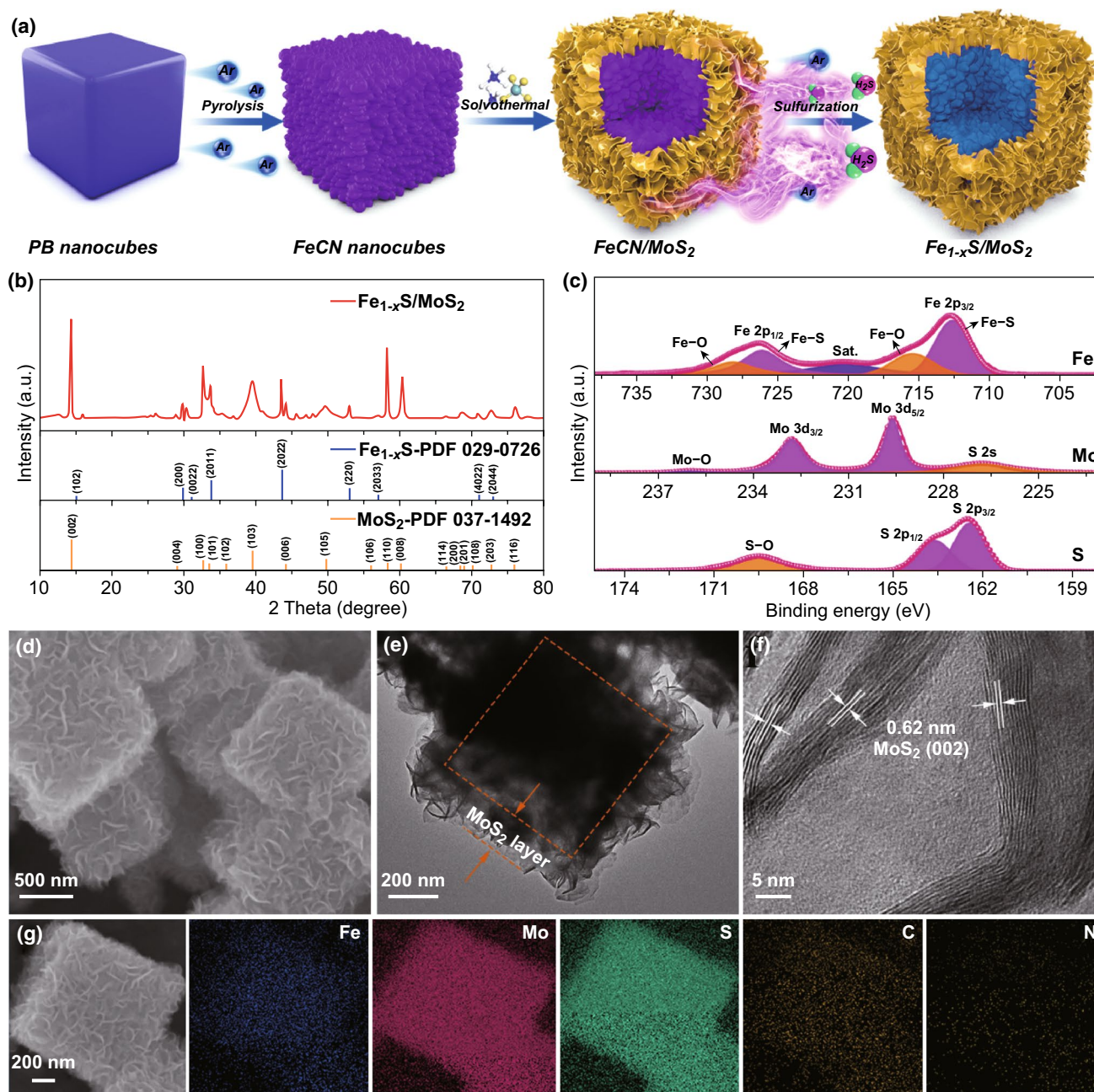
Fig. 1 **a** Schematic illustration of the synthesis process for $Fe_{1-x}S/MoS_2$ nanocomposite. **b** XRD pattern and **c** high-resolution XPS spectra (Fe 2*p*, Mo 3*d*, and S 2*p*) of $Fe_{1-x}S/MoS_2$ composite. **d** SEM, **e** TEM and **f** HRTEM images of $Fe_{1-x}S/MoS_2$ composite. **g** Element mappings of the $Fe_{1-x}S/MoS_2$ composite

nanocubic structure (FeCN) nanocubes in an inert atmosphere. As shown in Fig. S1c, the cubic framework is well maintained. MoS_2 nanosheets were then uniformly grown on surface of FeCN nanocubes, resulting in an enlarged nanocube size of about 1 μm (Fig. S1d). Finally, $Fe_{1-x}S/MoS_2$ composite was obtained without obvious structural change

after a sulfurization process (Fig. 1d). Figure 1b shows XRD pattern of the as-synthesized $Fe_{1-x}S/MoS_2$ composite. The diffraction peaks at 30.3°, 33.7°, 43.5° and 53.0° are assigned to the (200), (2011), (2022) and (220) planes of hexagonal pyrrhotite $Fe_{1-x}S$ (JCPDS NO. 29-0726), respectively. Besides, a series of strong peaks at 14.3°, 29.8°,

$32.7°$, $39.5°$, $44.2°$, $49.7°$, $58.2°$ and $60.3°$ can be readily indexed to the (002), (004), (100), (103), (006), (105), (110) and (008) planes of MoS_2 (JCPDS No. 37-1492). XPS analysis was performed to investigate the chemical compositions and surface electronic states of $Fe_{1-x}S/MoS_2$ composite. The survey spectra confirm the presence of Fe, Mo, S, C, and N elements (Fig. S2). In the Fe $2p$ XPS spectrum, the peaks located at 712.7 and 726.2 eV are corresponded to the Fe-S bonds along with a corresponding satellite at 720.3 eV, whereas the observed peaks at 715.5 and 728.2 eV indicate the presence of Fe–O bonds (Fig. 1c) [45]. In the S $2p$ XPS spectrum, peaks at 162.5 and 163.7 eV are correlated to the S $2p_{1/2}$ and S $2p_{3/2}$, respectively, while the peak centered at 169.4 eV is attributed to S–O bond from superficial oxidized sulfur species [46]. The Mo $3d$ XPS spectrum shows two obvious peaks at 229.6 and 232.8 eV corresponding to Mo $3d_{3/2}$ and Mo $3d_{5/2}$, respectively, which are the characteristic of Mo^{4+}, whereas the peak at 236.2 eV is attributed to Mo–O bond [47]. TEM image confirms that MoS_2 nanosheets are well anchored on the $Fe_{1-x}S$ nanocubes, and there is an obvious interface between the $Fe_{1-x}S$ and MoS_2 (Fig. 1e). The average thickness of MoS_2 is revealed to be around 150 nm, well consistent with SEM observation. High-resolution TEM image shows well-resolved lattice fringes with d-spacing of 0.62 and 0.23 nm, corresponding to the (002) and (103) planes of MoS_2, respectively (Fig. 1f). No obvious lattice fringes of $Fe_{1-x}S$ can be observed due to the coverage of thick MoS_2 nanosheets. EDS elemental mapping images manifest the existence of Fe, Mo, S, C, and N elements, further confirming the successful synthesis of $Fe_{1-x}S/MoS_2$ heterostructure (Fig. 1g). The existence of C and N elements could be attributed to the formation of N-doped carbon, which is expected to enhance the electronic conductivity of electrode materials [48, 49]. For comparison, bare $Fe_{1-x}S$ nanocubes were also synthesized by the same route without MoS_2. As shown in Fig. S3a, all diffraction peaks of $Fe_{1-x}S$ could be ascribed to the hexagonal pyrrhotite $Fe_{1-x}S$ (JCPDS NO. 29-0726) without any other impurity phases. SEM and TEM images show that the nanocubic-shaped morphology is well retained with a much rougher surface and porous structure (Fig. S3b-e). HRTEM image clearly displays the lattice spacing of 0.29 nm, corresponding to (200) plane of $Fe_{1-x}S$ (Fig. S3f). In addition, the nitrogen adsorption–desorption isotherms in Fig. S4 indicate that $Fe_{1-x}S/MoS_2$ composite possesses higher BET surface area of 45.6 m^2 g^{-1} than that of pure $Fe_{1-x}S$ (12.5 m^2 g^{-1}) (Fig. S4). The composite

structures with high porosity can provide abundant contact area and diffusion channels for electrolyte.

Figure 2a shows the CV curves of $Fe_{1-x}S/MoS_2$ heterostructure for the first five cycles. During the first discharge process, three obvious cathodic peaks at around 1.10, 0.60, and 0.15 V can be assigned to the multistep sodiation processes involving the intercalation of Na^+ into $Fe_{1-x}S/MoS_2$ and the formation of Mo^0/Fe^0 [13, 35, 50]. Meanwhile, the strong peak at about 0.60 V is also associated with the formation of SEI films, and the peak intensity decreases obviously in the subsequent cycles [38, 51]. For the anodic scan, two obvious peaks at about 1.60 and 1.90 V correspond to the stepwise desodiation process [52]. From the second cycle onward, the reversible reactions of $Na_{2-y}Fe_{1-x}S_2/Na_2Fe_{1-x}S_2$ and MoS_2/Mo^0 enable the reversible Na storage in composite electrode [12, 53]. These peaks related to the phase transformation during sodiation/desodiation process will be further discussed on the basis of in situ XRD analysis. The CV curves of $Fe_{1-x}S/MoS_2$ composite electrode basically overlap from the second cycle onward, indicating excellent electrochemical reversibility and structural stability of the heterostructure. In contrast, bare $Fe_{1-x}S$ nanocubes show inferior electrochemical reversibility (Fig. S5).

Figure 2b presents the galvanostatic charge–discharge curves of $Fe_{1-x}S/MoS_2$ composite electrode under different cycles at 100 mA g^{-1}. The $Fe_{1-x}S/MoS_2$ composite exhibits an initial discharge and charge capacities of 1072.1 and 645.0 mAh g^{-1}, respectively, showing an initial Coulombic efficiency of 60%. The irreversible capacity loss arises from the formation of SEI layer on the electrode surface [54]. However, the bare $Fe_{1-x}S$ electrode delivers a lower initial Coulombic efficiency of 58% at the same current density (Fig. S6). After 100 cycles, the $Fe_{1-x}S/MoS_2$ heterostructure demonstrates a high reversible capacity of 584.7 mAh g^{-1} with capacity retention of approximately 91%, and high Coulombic efficiency from the second cycle onward (Fig. 2c). In contrast, the bare $Fe_{1-x}S$ shows rapid capacity decay and lower Coulombic efficiency during the whole process.

The superiority of the heterostructure is also highlighted by its outstanding rate capability. The $Fe_{1-x}S/MoS_2$ composite electrode delivers the average reversible specific capacities of 637.2, 594.7, 552.8, 490.4, 432.3, and 372.1 mAh g^{-1} at the current densities of 0.1, 0.2, 0.5, 1.0, 2.0, and 3.0 A g^{-1}, respectively. When the current density returns to 0.1 A g^{-1}, the specific capacity can revert back to a high value of 636.7 mAh g^{-1} with approximately 100%
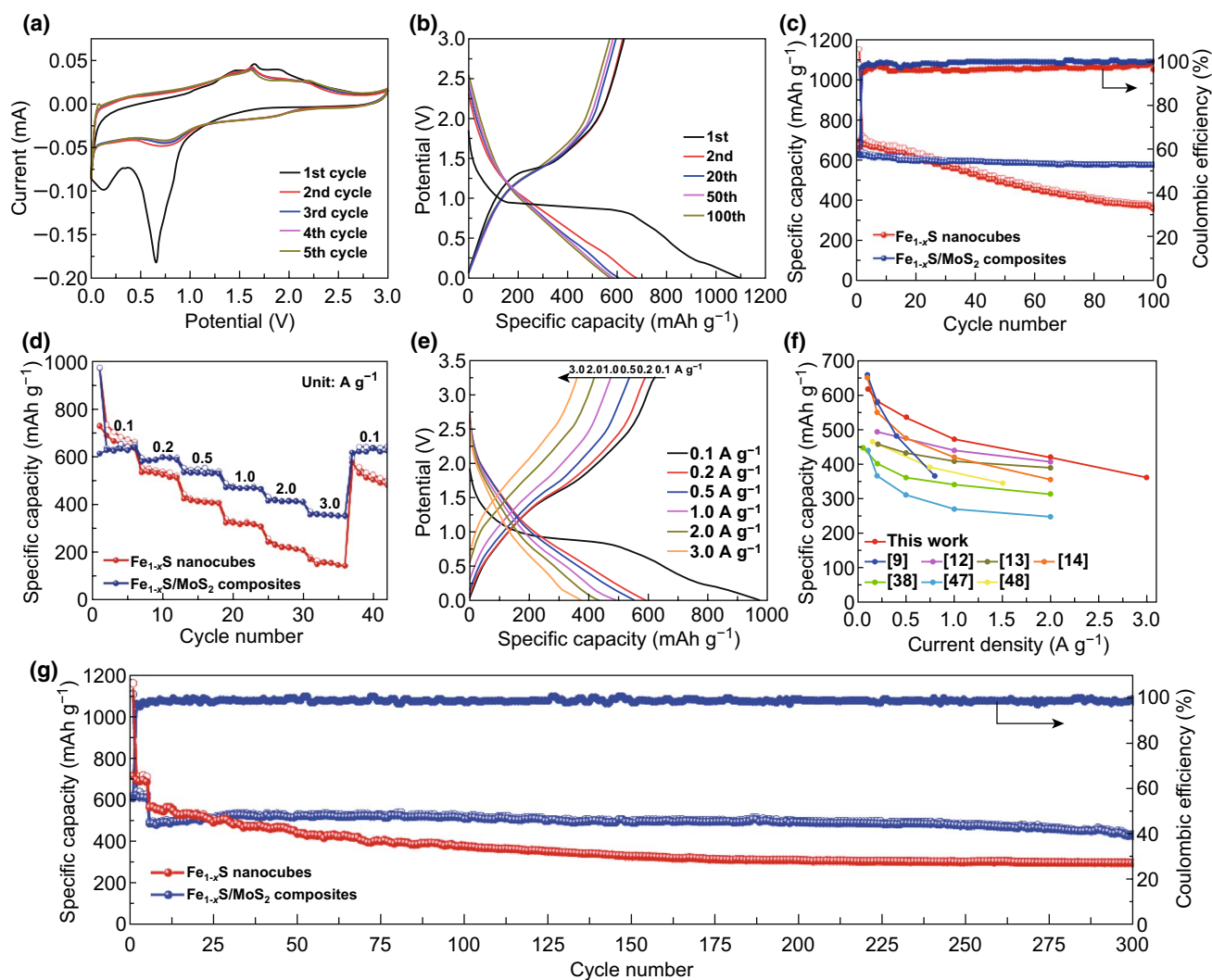
Fig. 2 **a** CV curves of $Fe_{1-x}S/MoS_2$ composite electrode for the first five cycles. **b** Galvanostatic charge–discharge profiles of $Fe_{1-x}S/MoS_2$ composite electrode at 100 mA g^{-1}. **c** Cycling performance at 100 mA g^{-1}. **d** Rate capability at various current densities. **e** Galvanostatic charge–discharge profiles of $Fe_{1-x}S/MoS_2$ composite electrode at various current densities. **f** The comparison of the rate capability with other iron sulfide-based anode materials previously reported [9, 12–14, 38, 55, 56]. **g** Long-term cycling performance at 1.0 A g^{-1}

capacity retention (Fig. 2d, e). Such excellent rate capability is superior to most of other iron sulfide-based anode materials reported previously, as shown in Fig. 2f. However, with the increasing current density, the bare $Fe_{1-x}S$ electrode shows a much lower capacity (Fig. S7). Furthermore, the long-term cycling performance of the $Fe_{1-x}S/MoS_2$ electrode was evaluated at 1.0 A g^{-1} (Fig. 2g) with an initial five cycles activation at 0.1 A g^{-1}. After 300 cycles, a high reversible capacity of 396.8 mAh g^{-1} is achieved, implying the superior high-rate cycling stability. However, the bare $Fe_{1-x}S$ electrode shows rather poor cycle performance under the identical testing conditions. *Ex situ* SEM was then

conducted after cycling. As shown in Fig. S8, $Fe_{1-x}S/MoS_2$ composite almost maintains the structural integrity without obvious damage, confirming the good structural stability for sodium storage. Such excellent cycling and rate performance might be related to the following unique hetero-nanostructure design advantages. First, the porous MoS_2 nanosheets enlarge the electrode/electrolyte contact area and reduce the charge-transfer resistance along the electrode/electrolyte interface. Second, the heterostructure structure design prevents the nanocubes agglomeration and accommodates the severe structural deformation significantly [35]. More importantly, the heterointerface between the $Fe_{1-x}S$ and

MoS$_2$ could serve as an "ion reservoir" to significantly boost Na$^+$ capture/storage and then accelerate the Na$^+$ diffusion from the shell to the internal part [31].

To further interpret the outstanding sodium storage performance of Fe$_{1-x}$S/MoS$_2$ heterostructure, kinetics analysis based on CV measurements at different scan rates was carried out. As shown, the CV curves from 0.1 to 1.0 mV s^{-1} exhibit similar shape with broad reduction/oxidation peaks related to the sodiation/desodiation processes (Fig. S9). The relationship between the peak current (i) and scan rate (v) obeys the power law as shown in Eq. (1) [57]:

$$i = av^b \qquad (1)$$

where both a and b are constants. The b value reveals the charge storage mechanism ($b = 0.5$ represents a diffusion-controlled process; $b = 1.0$ refers to a surface capacitance-controlled process). As shown in Fig. 3a, the b values obtained from the log (v) versus log (i) plots for peak 1, 2, 3, and 4 are 0.84, 0.92, 0.89, and 0.92, respectively, suggesting the charge storage in Fe$_{1-x}$S/MoS$_2$ composite is dominated by surface capacitive behavior.

To be more intuitive, the quantitative pseudocapacitance contribution at different scan rates could be calculated according to Eq. (2) [58]:
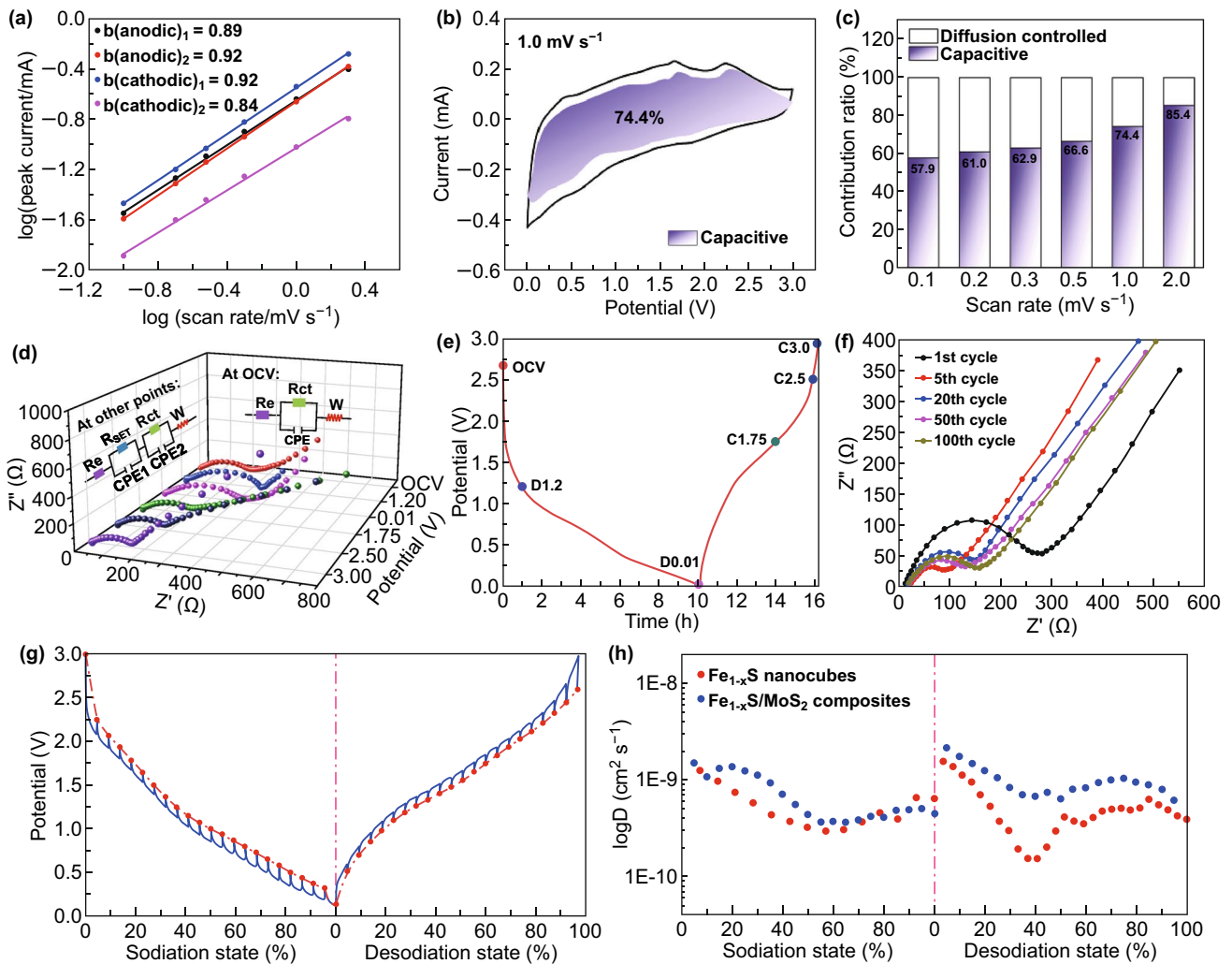
Fig. 3 Kinetic analysis of sodium storage behavior for Fe$_{1-x}$S/MoS$_2$ composite. **a** Linear relationship between log (i) and log (v). **b** Capacitive and diffusion-controlled contribution at 1.0 mV s^{-1}. **c** Normalized contribution ratio of capacitive capacities at different scan rates. **d** In situ EIS spectra evolution at different charge/discharge potentials. **e** First charge/discharge profile at 100 mA g^{-1} with labeled points for EIS. **f** EIS spectra after different cycles. **g** GITT curve. **h** The corresponding Na$^+$ diffusion coefficient at different discharge/charge state of Fe$_{1-x}$S/MoS$_2$ composite and pure Fe$_{1-x}$S electrodes

$$i(V) = k_1 v + k_2 v^{1/2} \tag{2}$$

where k_1 and k_2 are constants for a fixed voltage. The $k_1 v$ indicates the current response from surface capacitive contribution, while $k_2 v^{1/2}$ represents the diffusion-controlled current. The surface capacitive contribution of the $Fe_{1-x}S/MoS_2$ composite electrode at 1.0 mV s^{-1} is about 74.4% as displayed by the shaded area (Fig. 3b). With the increase in scan rate, the pseudocapacitance contribution gradually increases from 57.9% to 85.4% (Fig. 3c). However, the bare $Fe_{1-x}S$ electrode shows a much lower capacitive contribution at different scan rates (Fig. S8). The higher pseudocapacitance contribution for $Fe_{1-x}S/MoS_2$ composite determines a more favorable electrochemical kinetics behavior at high current density, which is consistent with its excellent rate capability as shown in Fig. 2.

In situ electrochemical impedance spectroscopy (EIS) during the first sodiation/desodiation process was conducted to investigate the kinetics differences induced by structural and phase evolution at different discharge/charge states. Figure 3d shows the EIS behavior of $Fe_{1-x}S/MoS_2$ composite in the first cycle with labeled points presented in Fig. 3e. All Nyquist plots show similar features with a depressed semicircle in high–medium-frequency region and an oblique line in low-frequency region. Based on the fitted equivalent circuits, at open-circuit voltage (OCV) state, the semicircle can be ascribed to the charge-transfer resistance (R_{ct}) and the oblique line represents the Warburg impedance (W) related to the Na$^+$ diffusion [59]. However, at other states, the semicircle corresponds to two overlapping parts of the SEI film resistance (R_{SEI}) and R_{ct} [60]. During the sodiation process, due to the formation of insulative Na$_2$S matrix and SEI films accompanied by the gradual volume change, the resistance increases obviously from OCV to 0.01 V [61]. During the desodiation process, the nanoclustered $Na_y Fe_{1-x} S_2$ phase and metallic state 1T-MoS_2 gradually form, and meanwhile, nonconductive Na$_2$S gradually disappears. As a consequence, the resistance decreases gradually from 0.01 to 3.0 V. In addition, EIS measurements were also performed after different cycles at current density of 100 mA g^{-1} to show the charge-transfer stability. With the increase in cycles, the resistance of $Fe_{1-x}S/MoS_2$ composite electrode decreases initially owing to the activation process and then slightly increases after several cycles (Fig. 3f). In contrast, Nyquist spectra of the bare $Fe_{1-x}S$ electrode show higher resistances at different cycles. Overall, the in situ EIS measurements have confirmed the enhanced charge-transfer

kinetics and electronic conductivity of the $Fe_{1-x}S/MoS_2$ composite (Fig. S10) [62, 63].

Galvanostatic intermittent titration technique (GITT) was further performed to investigate the influence of multistep sodiation and desodiation reactions of $Fe_{1-x}S/MoS_2$ heterostructure on Na-ion chemical diffusion coefficient (D_{Na}) (Figs. 3g and S12). From Fig. 3h, the Na$^+$ diffusion coefficient fluctuates with the progress of sodiation/desodiation, and the minimum values appear at each cathodic/anodic reaction plateau, where Na ions diffuse deeply into/from the internal crystal structure. Obviously, the $Fe_{1-x}S/MoS_2$ composite electrode shows a higher diffusion coefficient and minor change than those of bare $Fe_{1-x}S$, which can be attributed to the unique heterointerface to act as an "ion reservoir" and fast diffusion channel for Na ions. In addition, phase boundaries can suppress the growth of crystal domains, thus forming numerous defects and active sites to facilitate Na$^+$ diffusion [64]. Furthermore, benefiting from out-of-sync electrochemical reactions of these two sulfides at different voltages, the structural stress could be effectively mitigated, which is also favorable for diffusion of sodium ions.

To further reveal the voltage-dependent phase transformation behavior of $Fe_{1-x}S/MoS_2$ heterostructure during the first sodiation/desodiation process, in situ XRD was performed between 0.01 and 3.0 V at the current density of 80 mA g^{-1} (Fig. 4). Noticed that the strong peaks located at about 26.7°, 44.0°, and 46.0° are derived from carbon paper, BeO, and Be, respectively. As shown in Fig. 4, the peaks at 29.9°, 33.7°, and 43.5° are related to the (200), (2011), and (2022) planes of $Fe_{1-x}S$, and the peaks at about 14.3°, 32.7°, and 39.5° correspond to the (002), (100), and (103) diffractions of MoS_2. During the sodiation process, the peaks of $Fe_{1-x}S$ gradually shift to a lower 2θ, suggesting the formation of intermediate $Na_2Fe_{1-x}S_2$ through the Na$^+$ insertion into $Fe_{1-x}S$. When continuously discharging to 0.01 V, the peaks related to $Na_2Fe_{1-x}S_2$ gradually disappear, along with the gradual increase in the diffraction peak corresponding to Na$_2$S. Fe peaks could not be clearly observed in the process, which is mostly due to either the ultra-small crystal size or amorphous nature of resultant Fe^0 [65]. On the other hand, the prominent peak at 14.3° shifts obviously during the whole sodiation/desodiation process, indicating the structural changes of MoS_2. In stages I and II, there are two stages involving two-phase transitions: One is from 2H-MoS_2 ($2\theta_{(002)} = 14.3°$) to 2H-$Na_{0.5}MoS_2$ ($2\theta_{(002)} = 11.8°$) and the
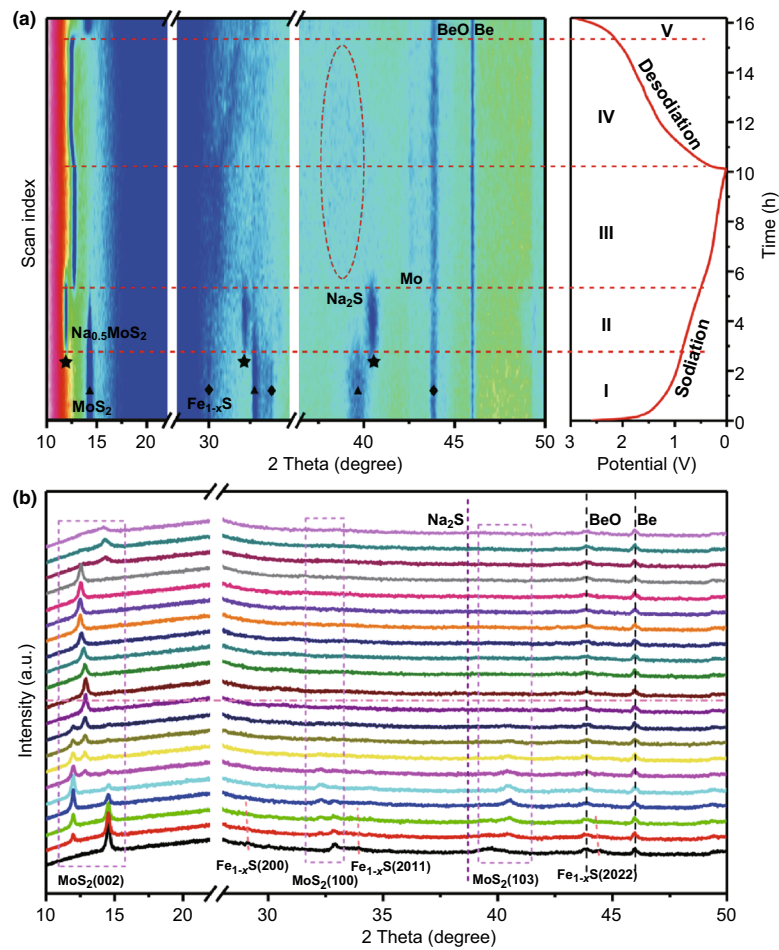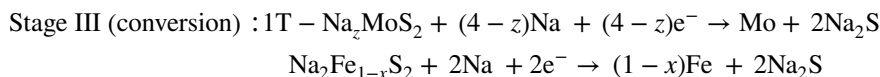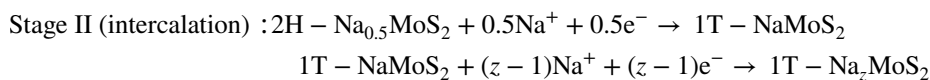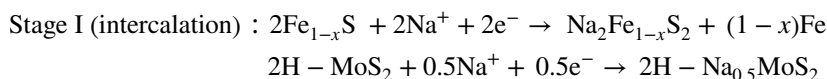
Fig. 4 **a** Contour plots of in situ XRD results and **b** selected diffraction patterns of $Fe_{1-x}S/MoS_2$ composite electrode during the first sodiation/desodiation process

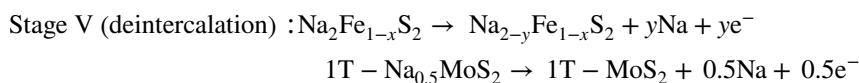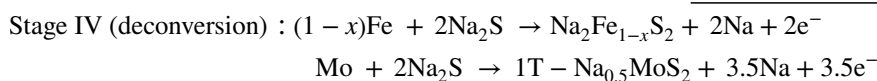other is from $2H-Na_{0.5}MoS_2$ to $1T-NaMoS_2$ ($2\theta_{(002)} = 12.6°$) [66]. Subsequently, more Na ions insertion into Na_zMoS_2 did not induce any detectable phase changes. In stage III, the intensity of diffraction peak related to Na_2S gradually increases accompanied by the formation of Mo. After recharging back to 1.6 V, the (002) main peak gradually shifts toward a lower 2θ angle to form $1T-NaMoS_2$. In subsequent deintercalation process, the diffraction peak shifts back to a higher 2θ angle with a two-phase transition from $1T-Na_{0.5}MoS_2$ to $1T-MoS_2$ ($2\theta_{(002)} = 14.1°$) rather than the initial $2H-MoS_2$ ($2\theta_{(002)} = 14.3°$) [47, 67]. Meanwhile, the diffraction peaks corresponding to Na_2S and Mo gradually

disappear. Interestingly, the diffraction peak related to Na_zMoS_2 always exists in the whole conversion reaction process, implying the incomplete conversion from Na_zMoS_2 to Mo, which is favorable for structural stability. At the desodiation process, due to the strong peak of carbon paper, the peaks at around 30° could not be clearly assigned to the $Na_2Fe_{1-x}S_2$ and $Na_{2-y}Fe_{1-x}S_2$, which are similar to the previous report for iron sulfide materials [12]. Therefore, from the above in situ XRD and CV analysis, the multistep reaction mechanisms for $Fe_{1-x}S/MoS_2$ heterostructure at different sodiation/desodiation states could be expressed as follows:

Sodiation process:

Stage I (intercalation) : $2Fe_{1-x}S + 2Na^+ + 2e^- \rightarrow Na_2Fe_{1-x}S_2 + (1-x)Fe$

$2H - MoS_2 + 0.5Na^+ + 0.5e^- \rightarrow 2H - Na_{0.5}MoS_2$

Stage II (intercalation) : $2H - Na_{0.5}MoS_2 + 0.5Na^+ + 0.5e^- \rightarrow 1T - NaMoS_2$

$1T - NaMoS_2 + (z-1)Na^+ + (z-1)e^- \rightarrow 1T - Na_zMoS_2$

Stage III (conversion) : $1T - Na_zMoS_2 + (4-z)Na + (4-z)e^- \rightarrow Mo + 2Na_2S$

$Na_2Fe_{1-x}S_2 + 2Na + 2e^- \rightarrow (1-x)Fe + 2Na_2S$

Desodiation process:

Stage IV (deconversion) : $(1-x)Fe + 2Na_2S \rightarrow Na_2Fe_{1-x}S_2 + 2Na + 2e^-$

$Mo + 2Na_2S \rightarrow 1T - Na_{0.5}MoS_2 + 3.5Na + 3.5e^-$

Stage V (deintercalation) : $Na_2Fe_{1-x}S_2 \rightarrow Na_{2-y}Fe_{1-x}S_2 + yNa + ye^-$

$1T - Na_{0.5}MoS_2 \rightarrow 1T - MoS_2 + 0.5Na + 0.5e^-$

Furthermore, the structural change of $Fe_{1-x}S/MoS_2$ composite electrode at a high current density was also monitored by in situ XRD. As shown in Fig. S13, from the second cycle forward, the (002) diffraction peak exhibits small periodic change, confirming the stable framework and kinetic processes of this composite structure during cycling.

DFT calculations were carried out to investigate the heterointerfacial behavior to present atomic-level verification for the superior sodium storage capability of the heterostructure. The Na^+ diffusion barriers in bare $Fe_{1-x}S$ and $Fe_{1-x}S/MoS_2$ heterostructure were calculated (Figs. 5b and S14). As shown, the barrier is about 0.4 eV in MoS_2 side close to the interface for heterostructure, obviously lower than that in bare $Fe_{1-x}S$ (~ 0.5 eV). This result indicates that Na^+ migration is more favorable in $Fe_{1-x}S/MoS_2$ heterointerface, which is beneficial for the improvement of electrochemical reaction kinetics. On the basis of the above analysis, a mechanism for enhanced electrochemical performance was proposed as illustrated in Fig. 5c. The $Fe_{1-x}S/MoS_2$ heterostructure is composed of hexagonal $Fe_{1-x}S$ nanocubes and 2D layered MoS_2 nanosheets. Once discharging, the unique "stacking card" nanostructures derived from the assembled MoS_2 nanosheets can accelerate the electrolyte permeation and Na^+ migration. Benefiting from the low diffusion barrier,

plenty of Na ions could store at the interface, then forming the so-called ion reservoir. High concentration gradient also drives Na^+ transport from the interface to the internal part, hence realizing an efficient conversion reaction kinetics [34]. After full sodiation, MoS_2 is transformed into metallic Mo and Na_2S. During the desodiation process, metallic Mo nanoclusters can serve as "pin conductor" until $1T-MoS_2$ phase is formed, dramatically improving the electrical conductivity of the whole electrode and then facilitating the conversion reaction [31]. In the subsequent cycles, such enhancement effects could be retained owing to the regeneration of heterointerface. The difference is that the original $2H-MoS_2$ phase was completely converted into $1T-MoS_2$ phase along with the change of electronic states between semiconductive and metallic, which can greatly enhance electrical conductivity, as well as boost Na^+ diffusion and accelerate the charge-transfer kinetics [67]. Therefore, such outstanding sodium storage performance can be mainly attributed to the unique heterostructure design: (1) Low Na^+ diffusion barrier originated from $Fe_{1-x}S/MoS_2$ heterointerface can significantly promote reaction kinetics; (2) the phase transformation from 2H- to $1T-MoS_2$ after the initial cycle can greatly enhance electrical conductivity; (3) nanoarchitectures enable shorten ion diffusion pathway
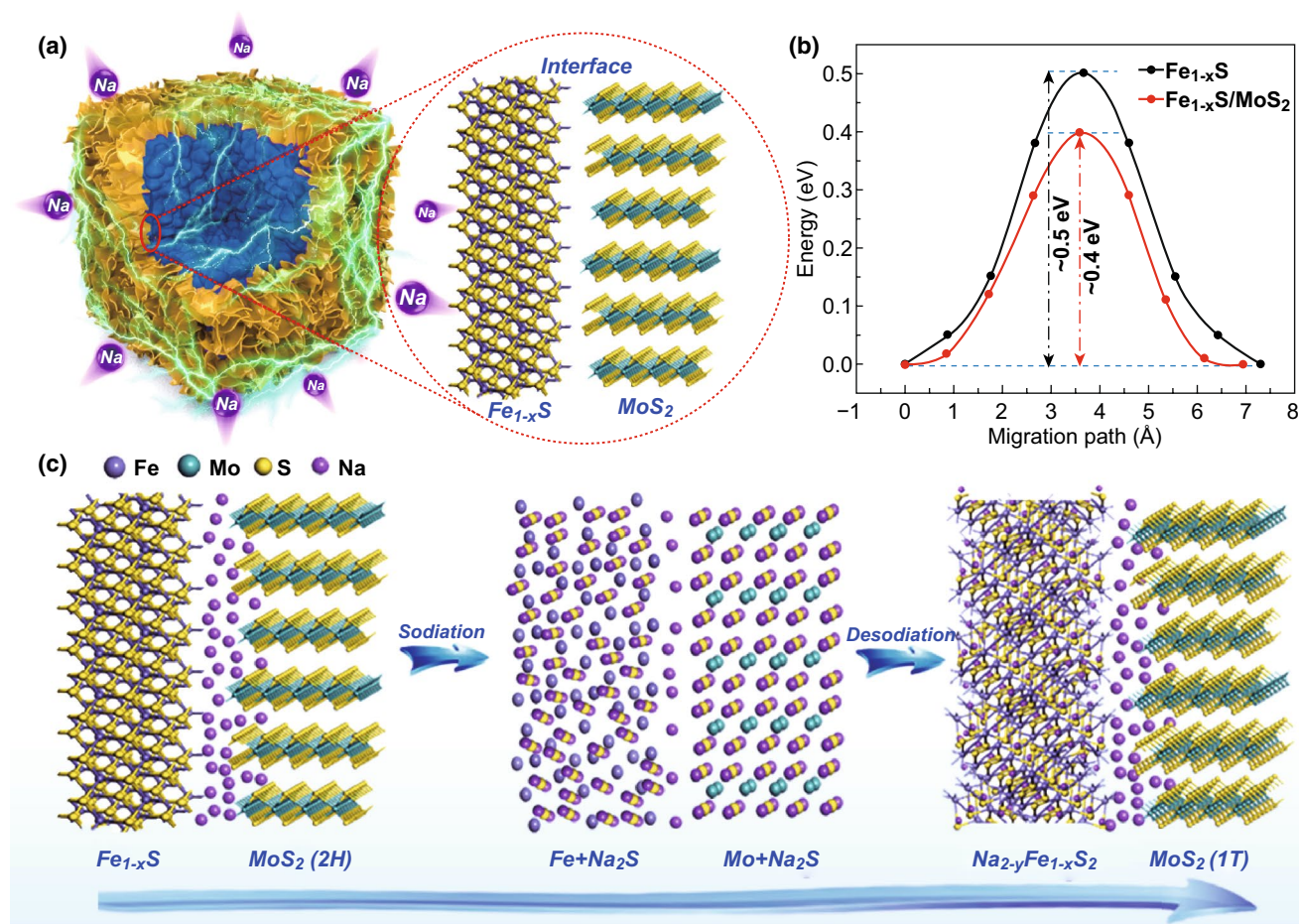
Fig. 5 **a** Schematic illustration of $Fe_{1-x}S/MoS_2$ interface. **b** The diffusion barrier profiles of Na on $Fe_{1-x}S$ surface and $Fe_{1-x}S/MoS_2$ interface. **c** Proposed schematic atomistic models of the illustrated reaction mechanism for $Fe_{1-x}S/MoS_2$ heterostructure during the sodiation and desodiation process

and mitigate the volume change; (4) high specific surface area caused by hierarchical MoS_2 nanosheet decoration is able to further buffer the structural stress and facilitate electrolyte permeation.

4 Conclusion

In conclusion, we have demonstrated experimental and theoretical evidence that the electrochemical reaction kinetics could be significantly boosted by rationally designing heterostructure with abundant "ion reservoir" for sodium storage. The low diffusion barrier at the heterointerface greatly promotes sodium ion diffusion and charge-transfer kinetics. As a proof of concept, SIB anode based on $Fe_{1-x}S/MoS_2$ heterostructure exhibits superior rate capability and long cycle life. In light

of the analysis about the dynamic relationship between heterointerface and electrochemical performance, our present work provides a fundamental understanding on heterostructure engineering for high-performance energy storage devices.

References

1. J.Y. Hwang, S.T. Myung, Y.K. Sun, Sodium-ion batteries: present and future. Chem. Soc. Rev. **46**, 3529 (2017). https://doi.org/10.1039/C6CS00776G

2. Y. Wang, D. Kong, W. Shi, B. Liu, G.J. Sim, Q. Ge, H.Y. Yang, Ice templated free-standing hierarchically WS_2/CNT-rGO aerogel for high-performance rechargeable lithium and sodium ion batteries. Adv. Energy Mater. **6**, 1601057 (2016). https://doi.org/10.1002/aenm.201601057

3. D. Kong, Y. Wang, Y.V. Lim, S. Huang, J. Zhang, B. Liu, T. Chen, H. Yang, 3D hierarchical defect-rich $NiMo_3S_4$ nanosheet arrays grown on carbon textiles for high-performance sodium-ion batteries and hydrogen evolution reaction. Nano Energy **49**, 460–470 (2018). https://doi.org/10.1016/j.nanoen.2018.04.051

4. Y. Wang, D. Kong, S. Huang, Y. Shi, M. Ding et al., 3D carbon foam supported WS_2 nanosheets for cable-shaped flexible sodium ion batteries. J. Mater. Chem. A **6**, 10813 (2018). https://doi.org/10.1039/C8TA02773K

5. S.P. Ong, V.L. Chevrier, G. Hautier, A. Jain, C. Moore, S. Kim, X. Ma, G. Ceder, Voltage, stability and diffusion barrier differences between sodium-ion and lithium-ion intercalation materials. Energy Environ. Sci. **4**, 3680–3688 (2011). https://doi.org/10.1039/c1ee01782a

6. Y. Zhao, A. Manthiram, Amorphous Sb_2S_3 embedded in graphite: a high-rate, long-life anode material for sodium-ion batteries. Chem. Commun. **51**, 13205–13208 (2015). https://doi.org/10.1039/C5CC03825A

7. L. Cao, B. Zhang, X. Ou, C. Wang, C. Peng, J. Zhang, Synergistical coupling interconnected ZnS/SnS_2 nanoboxes with polypyrrole-derived N/S dual-doped carbon for boosting high-performance sodium storage. Small **15**, 1804861 (2019). https://doi.org/10.1002/smll.201804861

8. W. Chen, X. Zhang, L. Mi, C. Liu, J. Zhang et al., High-performance flexible freestanding anode with hierarchical 3D carbon-networks/Fe_7S_8/graphene for applicable sodium-ion batteries. Adv. Mater. **31**, 1806664 (2019). https://doi.org/10.1002/adma.201806664

9. D. Li, D. Yang, X. Yang, Y. Wang, Z. Guo, Y. Xia, S. Sun, S. Guo, Double-helix structure in carrageenan-metal hydrogels: a general approach to porous metal sulfides/carbon aerogels with excellent sodium-ion storage. Angew. Chem. Int. Ed. **55**, 15925–15928 (2016). https://doi.org/10.1002/anie.201610301

10. J.K. Kim, S.K. Park, J.S. Park, Y.C. Kang, Uniquely structured composite microspheres of metal sulfides and carbon with cubic nanorooms for highly efficient anode materials for sodium-ion batteries. J. Mater. Chem. A **7**, 2636–2645 (2019). https://doi.org/10.1039/C8TA11481A

11. Y. Xiao, S.H. Lee, Y.K. Sun, The application of metal sulfides in sodium ion batteries. Adv. Energy Mater. **7**, 1601329 (2017). https://doi.org/10.1002/aenm.201601329

12. Y. Xiao, J.Y. Hwang, I. Belharouak, Y.K. Sun, Na storage capability investigation of a carbon nanotube-encapsulated $Fe_{1-x}S$ composite. ACS Energy Lett. **2**, 364–372 (2017). https://doi.org/10.1021/acsenergylett.6b00660

13. J. Xiang, Z. Liu, T. Song, Hierarchical iron sulfide-graphene nanocubes consisting of multiple nanoparticles with superior sodium ion storage properties. Electrochim. Acta **283**, 683–690 (2018). https://doi.org/10.1016/j.electacta.2018.07.017

14. Q. Pan, F. Zheng, X. Ou, C. Yang, X. Xiong, Z. Tang, L. Zhao, M. Liu, MoS_2 decorated $Fe_3O_4/Fe_{1-x}S$@C nanosheets as high-performance anode materials for lithium ion and sodium ion batteries. ACS Sustain. Chem. Eng. **5**, 4739–4745 (2017). https://doi.org/10.1021/acssuschemeng.7b00119

15. X. Xu, R. Zhao, W. Ai, B. Chen, H. Du et al., Controllable design of MoS_2 nanosheets anchored on nitrogen-doped graphene: toward fast sodium storage by tunable pseudocapacitance. Adv. Mater. **30**, 1800658 (2018). https://doi.org/10.1002/adma.201800658

16. D. Sun, D. Ye, P. Liu, Y. Tang, J. Guo, L. Wang, H. Wang, MoS_2/graphene nanosheets from commercial bulky MoS_2 and graphite as anode materials for high rate sodium-ion batteries. Adv. Energy Mater. **8**, 1702383 (2018). https://doi.org/10.1002/aenm.201702383

17. X. Xie, Z. Ao, D. Su, J. Zhang, G. Wang, MoS_2/graphene composite anodes with enhanced performance for sodium-ion batteries: the role of the two-dimensional heterointerface. Adv. Funct. Mater. **25**, 1393–1403 (2015). https://doi.org/10.1002/adfm.201404078

18. Y. Huang, Q. Pan, H. Wang, C. Ji, X. Wu, Z. He, Q. Li, Preparation of a $Sn@SnO_2@C@MoS_2$ composite as a high-performance anode material for lithium-ion batteries. J. Mater. Chem. A **4**, 7185–7189 (2016). https://doi.org/10.1039/C6TA02080A

19. H. Yin, S.H. Cheung, J.H.L. Ngai, C.H.Y. Ho, K.L. Chiu et al., Thick-film high-performance bulk-heterojunction solar cells retaining 90% PCEs of the optimized thin film cells. Adv. Electron. Mater. **3**, 1700007 (2017). https://doi.org/10.1002/aelm.201700007

20. H. Yin, P. Bi, S.H. Cheung, W.L. Cheng, K.L. Chiu et al., Balanced electric field dependent mobilities: a key to access high fill factors in organic bulk heterojunction solar cells. Sol. RRL **2**, 1700239 (2018). https://doi.org/10.1002/solr.201700239

21. X. Hong, J. Kim, S.F. Shi, Y. Zhang, C. Jin et al., Ultrafast charge transfer in atomically thin MoS_2/WS_2 heterostructures. Nat. Nanotechnol. **9**, 682–686 (2014). https://doi.org/10.1038/nnano.2014.167

22. H. Yin, S. Chen, S.H. Cheung, H.W. Li, Y. Xie et al., Porphyrin-based thick-film bulk-heterojunction solar cells for indoor light harvesting. J. Mater. Chem. C **6**, 9111–9118 (2018). https://doi.org/10.1039/C8TC02838A

23. Y. Ji, W. Guo, H. Chen, L. Zhang, S. Chen, M. Hua, Y. Long, Z. Chen, Surface Ti^{3+}/Ti^{4+} redox shuttle enhancing photocatalytic H_2 production in ultrathin TiO_2 nanosheets/CdSe quantum dots. J. Phys. Chem. C **119**, 27053–27059 (2015). https://doi.org/10.1021/acs.jpcc.5b09055

24. H. Yin, S. Chen, P. Bi, X. Xu, S.H. Cheung et al., Rationalizing device performance of perylenediimide derivatives as acceptors for bulk-heterojunction organic solar cells. Org. Electron. **65**, 156 (2019). https://doi.org/10.1016/j.orgel.2018.11.006

25. L. An, Z. Zhang, J. Feng, F. Lv, Y. Li et al., Heterostructure-promoted oxygen electrocatalysis enables rechargeable zinc-air battery with neutral aqueous electrolyte. J. Am. Chem. Soc. **140**, 17624–17631 (2018). https://doi.org/10.1021/jacs.8b09805

26. H. Yin, K.L. Chiu, C.H.Y. Ho, H.K.H. Lee, H.W. Li, Y. Cheng, S.W. Tsang, S.K. So, Bulk-heterojunction solar cells with enriched polymer contents. Org. Electron. **40**, 1–7 (2017). https://doi.org/10.1016/j.orgel.2016.10.030

27. Y. Wang, B. Hou, Y. Wang, H. Lu, J. Guo, Q. Ning, J. Zhang, C. Lu, X. Wu, Multiple heterointerfaces boosted de-/sodiation kinetics towards superior Na storage and Na-Ion full battery. J. Mater. Chem. A **6**, 6578–6586 (2018). https://doi.org/10.1039/C8TA01132J

28. X. Chang, T. Wang, P. Zhang, J. Zhang, A. Li, J. Gong, Enhanced surface reaction kinetics and charge separation of p-n heterojunction $Co_3O_4/BiVO_4$ photoanodes. J. Am. Chem. Soc. **137**, 8356–8359 (2015). https://doi.org/10.1021/jacs.5b04186

29. J. Nishitani, K.M. Yu, W. Walukiewicz, Charge transfer and mobility enhancement at CdO/SnTe heterointerfaces. Appl. Phys. Lett. **105**, 132103 (2014). https://doi.org/10.1063/1.4896912

30. H. Yin, J.K.W. Ho, S.H. Cheung, R.J. Yan, K.L. Chiu, X. Hao, S.K. So, Designing a ternary photovoltaic cell for indoor light harvesting with a power conversion efficiency exceeding 20%. J. Mater. Chem. A **6**, 8579–8585 (2018). https://doi.org/10.1039/C8TA01728J

31. J. Wang, J. Liu, H. Yang, D. Chao, J. Yan, S.V. Savilove, J. Lin, Z.X. Shen, MoS_2 nanosheets decorated $Ni_3S_2@MoS_2$ coaxial nanofibers: constructing an ideal heterostructure for enhanced Na-ion storage. Nano Energy **20**, 1–10 (2016). https://doi.org/10.1016/j.nanoen.2015.12.010

32. J. Wang, D. Chao, J. Liu, L. Li, L. Lai, J. Lin, Z. Shen, $Ni_3S_2@MoS_2$ core/shell nanorod arrays on Ni foam for high-performance electrochemical energy storage. Nano Energy **7**, 151–160 (2014). https://doi.org/10.1016/j.nanoen.2014.04.019

33. L. Fang, Z. Lan, W. Guan, P. Zhou, N. Bahlawane et al., Hetero-interface constructs ion reservoir to enhance conversion reaction kinetics for sodium/lithium storage. Energy Storage Mater. **18**, 107–113 (2019). https://doi.org/10.1016/j.ensm.2018.10.002

34. Y. Zheng, T. Zhou, C. Zhang, J. Mao, H. Liu, Z. Guo, Boosted charge transfer in SnS/SnO_2 heterostructures: toward high rate capability for sodium-ion batteries. Angew. Chem. Int. Ed. **55**, 3408–3413 (2016). https://doi.org/10.1002/anie.201510978

35. Z. Zhang, J. Zhao, M. Xu, H. Wang, Y. Gong, J. Xu, Facile synthesis of Sb_2S_3/MoS_2 heterostructure as anode material for sodium-ion batteries. Nanotechnology **29**, 335401 (2018). https://doi.org/10.1088/1361-6528/aac645

36. S. Dong, C. Li, X. Ge, Z. Li, X. Miao, L. Yin, $ZnS-Sb_2S_3@C$ core-double shell polyhedron structure derived from metal-organic framework as anodes for high performance sodium ion batteries. ACS Nano **11**, 6474–6482 (2017). https://doi.org/10.1021/acsnano.7b03321

37. H. Ming, N.L.K. Torad, Y.D. Chiang, K.C.W. Wu, Size- and shape-controlled synthesis of Prussian Blue nanoparticles by a polyvinylpyrrolidone-assisted crystallization process. CrystEngComm **14**, 3387–3396 (2012). https://doi.org/10.1039/c2ce25040c

38. G. Kresse, J. Joubert, From ultrasoft pseudopotentials to the projector augmented-wave method. Phys. Rev. B **59**(3), 1758–1775 (1999). https://doi.org/10.1103/PhysRevB.59.1758

39. P.E. Blöchl, Projector augmented-wave method. Phys. Rev. B **50**(24), 17953–17979 (1994). https://doi.org/10.1103/PhysRevB.50.17953

40. G. Kresse, J. Hafner, Ab initio molecular dynamics for liquid metals. Phys. Rev. B **47**(1), 558–561 (1993). https://doi.org/10.1103/PhysRevB.47.558

41. G. Kresse, J. Furthmuller, Efficient iterative schemes for ab initio total-energy calculations using a plane-wave basis set. Phys. Rev. B **54**(16), 11169–11186 (1996). https://doi.org/10.1103/PhysRevB.54.11169

42. J.P. Perdew, K. Burke, M. Ernzerhof, Generalized gradient approximation made simple. Phys. Rev. Lett. **77**, 3865–3868 (1996). https://doi.org/10.1103/PhysRevLett.77.3865

43. H.J. Monkhorst, J.D. Pack, Special points for Brillouin-zone integrations. Phys. Rev. B **13**(12), 5188–5192 (1976). https://doi.org/10.1103/PhysRevB.13.5188

44. G. Henkelman, B.P. Uberuaga, H. Jónsson, A climbing image nudged elastic band method for finding saddle points and minimum energy paths. J. Chem. Phys. **113**(22), 9901 (2000). https://doi.org/10.1063/1.1329672

45. B. Hou, Y. Wang, J. Guo, Q. Ning, X. Xi et al., Pseudocapacitance-boosted ultrafast Na storage in a pie-like FeS@C nanohybrid as an advanced anode material for sodium-ion full batteries. Nanoscale **10**, 9218–9225 (2018). https://doi.org/10.1039/C7NR09674G

46. X. Zhu, D. Liu, D. Zheng, G. Wang, X. Huang, J. Harris, D. Qu, D. Qu, Dual carbon-protected metal sulfides and their application to sodium-ion battery anodes. J. Mater. Chem. A **6**, 13294–13301 (2018). https://doi.org/10.1039/C8TA03444C

47. Q. Pan, Q. Zhang, F. Zheng, Y. Liu, Y. Li et al., Construction of MoS_2/C hierarchical tubular heterostructures for high-performance sodium ion batteries. ACS Nano **12**, 12578–12586 (2018). https://doi.org/10.1021/acsnano.8b07172

48. Z. Yang, P. Zhang, J. Wang, Y. Yan, Y. Yu, Q. Wang, M. Liu, Hierarchical carbon@SnS_2 aerogel with "skeleton/skin" architectures as a high-capacity, high-rate capability and long cycle life anode for sodium ion storage. ACS Appl. Mater. Interfaces **10**, 37434–37444 (2018). https://doi.org/10.1021/acsami.8b14861

49. B. Hou, Y. Wang, D. Liu, Z. Gu, X. Feng et al., N-doped carbon-coated $Ni_{1.8}Co_{1.2}Se_4$ nanoaggregates encapsulated in N-doped carbon nanoboxes as advanced anode with outstanding high-rate and low-temperature performance for sodium-ion half/full batteries. Adv. Funct. Mater. **28**, 1805444 (2018). https://doi.org/10.1002/adfm.201805444

50. Z. Liu, T. Lu, T. Song, X. Yu, X.W. Lou, U. Paik, Structure-designed synthesis of FeS_2@C yolk-shell nanoboxes as a high-performance anode for sodium-ion batteries. Energy Environ. Sci. **10**, 1576–1580 (2017). https://doi.org/10.1039/C7EE01100H

51. Q. Wang, W. Zhang, C. Guo, Y. Liu, C. Wang, Z. Guo, In situ construction of 3D interconnected FeS@Fe_3C@graphitic carbon networks for high-performance sodium-ion batteries. Adv. Funct. Mater. **27**, 1703390 (2017). https://doi.org/10.1002/adfm.201703390

52. W. Yu, C. Liu, L. Zhang, P. Hou, F. Li, B. Zhang, H. Cheng, Synthesis and electrochemical lithium storage behavior of carbon nanotubes filled with iron sulfide nanoparticles. Adv. Sci. **3**, 1600113 (2016). https://doi.org/10.1002/advs.201600113

53. D. Su, S. Dou, G. Wang, Ultrathin MoS_2 nanosheets as anode materials for sodium-ion batteries with superior performance. Adv. Energy Mater. **5**, 1401205 (2015). https://doi.org/10.1002/aenm.201401205

54. Y. Wang, B. Hou, J. Guo, Q. Ning, W. Pang, J. Wang, C. Lü, X. Wu, An Ultralong lifespan and low-temperature workable sodium-ion full battery for stationary energy storage. Adv. Energy Mater. **8**, 1703252 (2018). https://doi.org/10.1002/aenm.201703252

55. Z. Wu, J. Li, Y. Zhong, J. Liu, K. Wang et al., Synthesis of FeS@C-N hierarchical porous microspheres for the applications in lithium/sodium ion batteries. J. Alloys Compds. **688**, 790–797 (2016). https://doi.org/10.1016/j.jallcom.2016.07.268

56. X. Wei, W. Li, J. Shi, L. Gu, Y. Yu, FeS@C on carbon cloth as flexible electrode for both lithium and sodium storage. ACS Appl. Mater. Interfaces **7**, 27804–27809 (2015). https://doi.org/10.1021/acsami.5b09062

57. V. Augustyn, J. Come, M.A. Lowe, J.W. Kim, P.L. Taberna et al., High-rate electrochemical energy storage through Li^+ intercalation pseudocapacitance. Nat. Mater. **12**, 518–522 (2013). https://doi.org/10.1038/nmat3601

58. S. Huang, L. Liu, Y. Zheng, Y. Wang, D. Kong et al., Efficient sodium storage in rolled-up amorphous Si nanomembranes. Adv. Mater. **30**, 1706637 (2018). https://doi.org/10.1002/adma.201706637

59. P.K. Dutta, U.K. Sen, S. Mitra, Excellent electrochemical performance of tin monosulphide (SnS) as a sodium-ion battery anode. RSC Adv. **4**, 43155–43159 (2014). https://doi.org/10.1039/C4RA05851H

60. S. Chen, Z. Chen, Y. Luo, M. Xia, C. Cao, Silicon hollow sphere anode with enhanced cycling stability by a template-free method. Nanotechnology **28**, 165404 (2017). https://doi.org/10.1088/1361-6528/aa63a1

61. D. Chao, P. Liang, Z. Chen, L. Bai, H. Shen et al., Pseudocapacitive Na-ion storage boosts high rate and areal capacity of self-branched 2D layered metal chalcogenide nanoarrays. ACS Nano **10**, 10211–10219 (2016). https://doi.org/10.1021/acsnano.6b05566

62. S. Chen, Z. Chen, C. Cao, Mesoporous spinel $LiMn_2O_4$ cathode material by a soft-templating route. Electrochim. Acta **199**, 51–58 (2016). https://doi.org/10.1016/j.electacta.2016.03.135

63. S. Chen, Z. Chen, X. Xu, C. Cao, M. Xia, Y. Luo, Scalable 2D mesoporous silicon nanosheets for high-performance lithium-ion battery anode. Small **14**, 1703361 (2018). https://doi.org/10.1002/smll.201703361

64. G. Fang, Z. Wu, J. Zhou, C. Zhu, X. Cao et al., Pseudocapacitive effect and fast ion diffusion in bimetallic sulfides as an advanced sodium-ion battery anode. Adv. Energy Mater. **8**, 1703155 (2018). https://doi.org/10.1002/aenm.201703155

65. S. Huang, S. Fan, L. Xie, Q. Wu, D. Kong et al., Promoting highly reversible sodium storage of iron sulfide hollow polyhedrons via cobalt incorporation and graphene wrapping. Adv. Energy Mater. **9**, 1901584 (2019). https://doi.org/10.1002/aenm.201901584

66. X. Wang, X. Shen, Z. Wang, R. Yu, L. Chen, Atomic-scale clarification of structural transition of MoS_2 upon sodium intercalation. ACS Nano **8**, 11394–11400 (2014). https://doi.org/10.1021/nn505501v

67. P. Gao, L. Wang, Y. Zhang, Y. Huang, K. Liu, Atomic-scale probing of the dynamics of sodium transport and intercalation-induced phase transformations in MoS_2. ACS Nano **9**, 11296–11301 (2015). https://doi.org/10.1021/acsnano.5b04950